On the Modeling of Prismatic Joints in Flexible Multi-Body Systems *

O.A. Bauchau
Georgia Institute of Technology,
School of Aerospace Engineering.
Atlanta, Georgia, 30332, USA.

Abstract

This paper focuses on the modeling of prismatic joints in flexible multi-body systems. In the classical formulation of prismatic joints for rigid bodies, kinematic constraints are enforced between the kinematic variables of the two bodies. These constraints express the conditions for relative translation of the two bodies along a body fixed axis, and imply the relative sliding of the two bodies which remain in constant contact with each other. However, these kinematic constraints no longer imply relative sliding with contact when one of the bodies is flexible. To remedy this situation, a *sliding joint* is proposed that involves kinematic constraints at the instantaneous point of contact between the sliding bodies. Various numerical examples are presented that demonstrate the dramatically different behavior of prismatic and sliding joints in the presence of elastic bodies.

1 Introduction

This paper is concerned with the dynamic analysis of flexible, nonlinear multi-body systems, *i.e.* a collection of bodies in arbitrary motion with respect to each other while each body is undergoing large displacements and rotations with respect to a body attached frame of reference. The focus is on problems where the strains within each elastic body remain small.

The elastic bodies are modeled using the finite element method. Beam elements will be the focus of this paper. The location of each node of the beam is represented by its Cartesian coordinates in an inertial frame, and the rotation of the cross-section at each node is represented by a finite rotation tensor expressed in the same inertial frame. The kinematic constraints among the various bodies are enforced via the Lagrange multiplier technique. Although this approach does not involve the minimum set of coordinates, it allows a modular development of finite elements for the enforcement of the kinematic constraints.

A distinguishing feature of multi-body systems is the presence of joints which impose different types of kinematic constraints between the various bodies of the system. An exhaustive classification of these joint types can be found in text books, such as [1], for instance. This paper will focus on the modeling of prismatic joints. A prismatic joint, schematically depicted in fig. 1, allows the relative translation of two bodies, denoted body k and l, respectively, about an axis fixed with respect to body k, while no relative rotation is allowed between the bodies.

At first, we focus on the case where body l is a rigid body. Fig. 1 depicts the prismatic joint in the reference and deformed configurations. In the reference configuration, the prismatic joint is

* *Computer Methods in Applied Mechanics and Engineering*, **181**, pp 87-105, 2000.

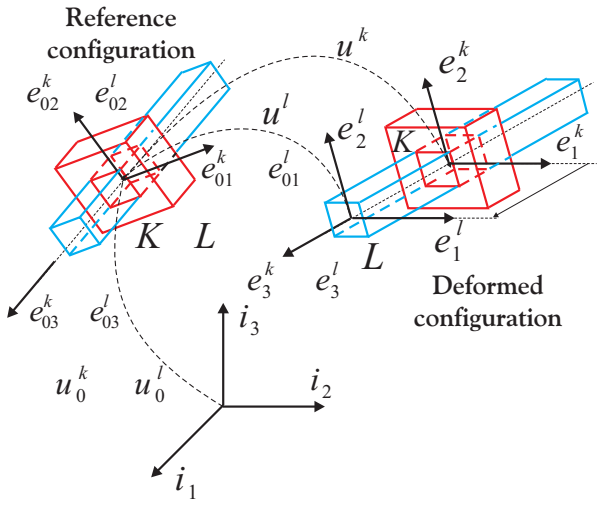

Figure 1: Prismatic joint in the reference and deformed configurations.

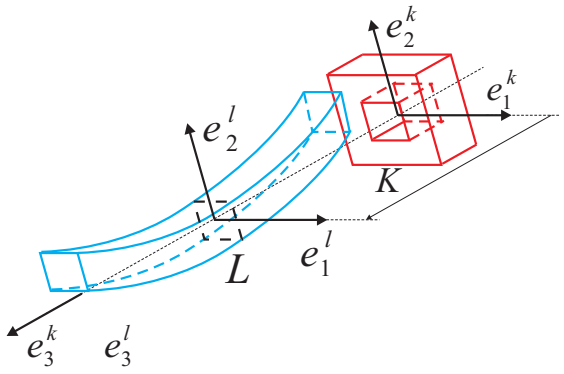

Figure 2: Prismatic joint with a flexible body.

defined by coincident triads $\mathcal{S}_0^k = \mathcal{S}_0^l$, attached to points K and L, respectively, which are material points on body k and l, respectively. In the deformed configuration, the orientations of triads $\mathcal{S}^k$ and $\mathcal{S}^l$ are still identical, but their origins are different: body l translated a distance Δ with respect to body k in the direction $\vec{e}_3{}^k = \vec{e}_3{}^l$. The first set of kinematic constraints associated with the prismatic joint is

$$\underline{e}_1^{lT}\ \underline{u} = \underline{e}_2^{lT}\ \underline{u} = 0, \tag{1}$$

and imply the orthogonality of both $\vec{e}_1{}^l$ and $\vec{e}_2{}^l$ to $\vec{u} = \vec{u}\,^l - \vec{u}\,^k$, the vector joining points K and L. The second set of constraints writes

$$\underline{e}_1^k = \underline{e}_1^l; \quad \underline{e}_2^k = \underline{e}_2^l; \quad \underline{e}_3^k = \underline{e}_3^l, \tag{2}$$

and imply identical orientations for triads $\mathcal{S}^k$ and $\mathcal{S}^l$. Finally, the relative translation of the bodies is $\Delta = \underline{e}_3^{lT}\ \underline{u}$, the projection of vector $\vec{u}$ along $\vec{e}_3{}^l$. It is important to note that although these constraints are expressed in terms of the kinematic variables at points K and L, they imply the sliding of body l on body k at point K, *when body l is rigid*.

The situation is sharply different when body l is flexible, as shown in fig. 2. If conditions (1) and (2) are enforced, body l is no longer sliding on body k at point K, *i.e.* contact between the bodies is no longer enforced. In actual systems, the piece of hardware corresponding to the prismatic joint implies the sliding of body l on body k with contact at point K at all times, as depicted in fig. 3. In fact, in the presence of flexible bodies, such joint is more accurately described as a *sliding joint*.

Due to the flexibility of body l, the kinematic variables at material points K and L are no longer related by conditions (1) and (2). Rather, constraint conditions must be enforced between the

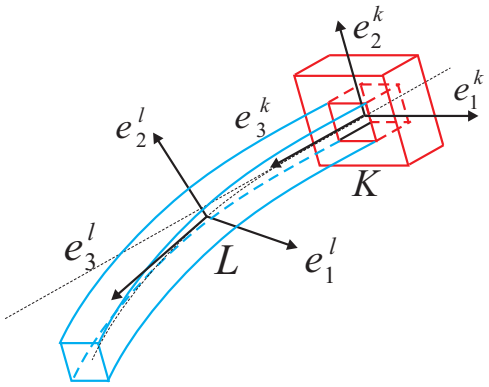

Figure 3: Sliding joint with a flexible body.

kinematic variables at point K of body k, and the kinematic variables at the material point of body l which is in contact with body k at an instant. Clearly, kinematic constraints (1) and (2) associated with the classical formulation of prismatic joints, and the kinematic constraint associated with sliding in the presence of flexible bodies are fundamentally different and will lead to sharply different dynamic responses of the system. Although the above discussion has focused on prismatic joints, it is clear that identical remarks can be made concerning the classical formulation of cylindrical joints, and about their inadequacy to model sliding behavior in the presence of flexible bodies.

This paper is organized in the following manner. The classical formulation of prismatic joints will be described in section 3. In section 4, the formulation of a simple, yet effective sliding joint is proposed. This joint involves the sliding of a node of a body along a flexible beam element. The nonlinear holonomic constraints associated with both prismatic and sliding joints in multi-body systems will be formulated within the framework of the energy preserving and decaying schemes introduced in [2, 3, 4, 5]. In these schemes, unconditional stability is achieved for nonlinear elastic multi-body systems by combining two features: an energy preservation or decay statement for the elastic bodies of the system, and the vanishing of the work done by the forces of constraint. The use of these unconditionally stable schemes is of particular importance in systems with prismatic and sliding joints whose dynamic response varies very rapidly due to the complex nature of the constraint conditions and to the moving contact point in sliding joints. In section 5, numerical examples are presented that demonstrate the sharp difference between the dynamic response of the prismatic and sliding joints in the presence of flexible bodies. The versatility of the proposed sliding joint is also demonstrated. An automated time step size selection procedure developed in [3] is used to obtain accurate solutions in an efficient manner.

2 Kinematic notations and conventions

The kinematic description of bodies and joints in their reference and deformed configurations will make use of three orthogonal triads. First, an inertial triad is used as a global reference for the system; it is denoted $\mathcal{S}_I$ with unit vectors $\vec{\imath}_1$, $\vec{\imath}_2$, and $\vec{\imath}_3$. A second triad $\mathcal{S}_0$, with unit vectors $\vec{e}_{01}$, $\vec{e}_{02}$, and $\vec{e}_{03}$ is attached to the body and defines its orientation in the reference configuration. Finally, a third triad $\mathcal{S}^*$ with unit vectors $\vec{e}_1$, $\vec{e}_2$, and $\vec{e}_3$ defines the orientation of the body in its deformed configuration.

Let $\vec{u}_0$ and $\vec{u}$ be the displacement vectors from $\mathcal{S}_I$ to $\mathcal{S}_0$, and $\mathcal{S}_0$ to $\mathcal{S}^*$, respectively, and $\mathbf{R}_0$ and $\mathbf{R}$ the rotation tensors from $\mathcal{S}_I$ to $\mathcal{S}_0$, and $\mathcal{S}_0$ to $\mathcal{S}^*$, respectively. In this work, all vector and tensor components are measured in either $\mathcal{S}_I$ or $\mathcal{S}^*$. For instance, the components of vector $\vec{u}$ measured in $\mathcal{S}_I$ and $\mathcal{S}^*$ will be denoted $\underline{u}$ and $\underline{u}^*$, respectively, and clearly

$$\underline{u}^* = R_0^T R^T \ \underline{u}. \tag{3}$$

Similarly, the components of tensor $\mathbf{R}$ measured $\mathcal{S}_I$ and $\mathcal{S}^*$ will be denoted R and R^*, respectively. The skew-symmetric matrix formed with the components $\underline{u}$ will be denoted $\widetilde{u}$.

3 The prismatic joint

Consider two bodies denoted with superscripts $(.)^k$ and $(.)^l$, respectively, linked together by a prismatic joint, as depicted in fig. 1. In the reference configuration, the prismatic joint is defined by two coincident triads $\mathcal{S}_0^k = \mathcal{S}_0^l$. In the deformed configuration, no relative rotations are allowed and the corresponding triads are allowed to translate with respect to each other in such a way that $\vec{e}_3^{\,k} = \vec{e}_3^{\,l}$. This condition implies the orthogonality of both $\vec{e}_1^{\,l}$ and $\vec{e}_2^{\,l}$ to vector $\vec{u} = \vec{u}^{\,l} - \vec{u}^{\,k}$ which

joins the origin of the two triads. These two kinematic constraints are

$$\mathcal{C}_\alpha = \underline{e}_\alpha^{lT}\ \underline{u} = 0, \tag{4}$$

with $\alpha = 1$ and 2, respectively. Of course, in the deformed configuration, the orientation of the two triads is still identical; this constraint is readily enforced within the framework of finite element formulations by Boolean identification of the corresponding degrees of freedom. The relative displacement Δ of the prismatic joint is defined by adding a third constraint

$$\mathcal{C}_3 = \underline{e}_3^{lT}\ \underline{u} - \Delta = 0, \tag{5}$$

which expresses the relative displacement of the bodies as the projection of $\vec{u}$ along $\vec{e}_3^{\,l}$. As discussed in [2], holonomic constraints are enforced by the addition of a constraint potential $\lambda\,\mathcal{C}$, where λ is the Lagrange multiplier. The forces of constraint $\underline{\mathcal{F}}^c$ corresponding to eqs. (4) or (5) are readily obtained as

$$\delta\mathcal{C}\cdot\lambda = \begin{bmatrix} \delta\underline{u}^k \\ \delta\underline{u}^l \\ \hline \delta\psi^l \\ \hline \delta\Delta \end{bmatrix}^T \cdot \begin{bmatrix} - & \lambda & \underline{e}_\alpha^l \\ & \lambda & \underline{e}_\alpha^l \\ & \lambda & \widetilde{e}_\alpha^{\,l}\ \underline{u} \\ - & \lambda & \end{bmatrix} = \begin{bmatrix} \delta\underline{u}^k \\ \delta\underline{u}^l \\ \hline \delta\psi^l \\ \hline \delta\Delta \end{bmatrix}^T \cdot \underline{\mathcal{F}}^c, \tag{6}$$

where the virtual rotations are defined as $\widetilde{\delta\psi} = \delta R\ R^T$; $\alpha = 1$, 2, and 3 for the three constraints, respectively; and the last line in the constraint force expression is omitted for the first two constraints. To obtain unconditionally stable schemes for constrained systems, these forces of constraint must be discretized so that the work they perform vanishes exactly. The following discretization is proposed

$$\underline{\mathcal{F}}_m^c = \begin{bmatrix} - & s\lambda_m & \underline{e}_{\alpha m}^l \\ & s\lambda_m & \underline{e}_{\alpha m}^l \\ & s\lambda_m & \widetilde{e}_{\alpha m}^{\,l}\ \underline{u}_m \\ - & s\lambda_m & \end{bmatrix}, \tag{7}$$

where s is a scaling factor for the Lagrange multipliers, λ_m the unknown mid-point value of this multiplier, and

$$\underline{e}_{\alpha m} = \frac{\underline{e}_{\alpha f} + \underline{e}_{\alpha i}}{2}; \quad \underline{u}_m = \frac{\underline{u}_f + \underline{u}_i}{2}. \tag{8}$$

In these expressions, the subscripts $()_i$ and $()_f$ refer to the values of the corresponding variables at the initial and final times of the time step, respectively. The discretization of the finite rotations is discussed in Appendix B. The work done by these constraint forces during the time step is computed as follows

$$\begin{aligned} \Delta\mathcal{W}^c &= s\lambda_m\ \left[(\underline{u}_f - \underline{u}_i)\ \underline{e}_{\alpha m}^l + \underline{r}^{lT}\ \widetilde{e}_{\alpha m}^{\,l}\ \underline{u}_m - (\Delta_f - \Delta_i)\right] \\ &= s\lambda_m\ \left[(\underline{u}_f - \underline{u}_i)\ \underline{e}_{\alpha m}^l + \underline{i}_\alpha^T\ R_0^T R_m^{lT}\ \frac{G + G^T}{2}\ \widetilde{r}^{lT}\ \underline{u}_m - (\Delta_f - \Delta_i)\right] \\ &= s\lambda_m\ (\mathcal{C}_f - \mathcal{C}_i), \end{aligned} \tag{9}$$

where $\underline{r}$ is the incremental rotation parameterized using Rodrigues parameters, see Appendix A, and the last equality was obtained with the help of eq. (A5). It is now clear that the work done by the discretized constraint forces vanishes if $\mathcal{C}_f - \mathcal{C}_i = 0$. In order to avoid the drift phenomenon, it is preferable to enforce the condition $\mathcal{C}_f = 0$ at each time step. In summary, discretization (7) together with the constraint $\mathcal{C}_f = 0$ leads to the vanishing of the work done by the forces of constraint. This energy preserving formulation can be readily extended to an energy decaying formulation by following the steps outlined in section 4.3 of [2].

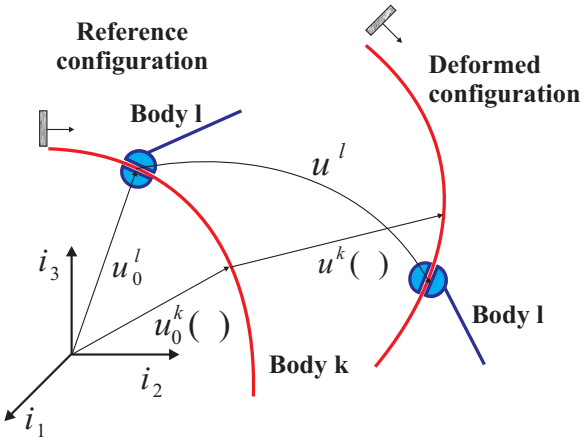

Figure 4: Sliding joint in the reference and deformed configurations.

4 The sliding joint

Consider two bodies denoted with superscripts $(.)^k$ and $(.)^l$, respectively, linked together by a sliding joint, as depicted in fig. 4. Body k is a flexible beam element whose displacement field is interpolated from nodal quantities, in a typical finite element manner. In the reference configuration, the coordinates of a point on the beam are

$$\underline{u}_0^k(\eta) = h^\alpha(\eta)\ \underline{u}_0^{k\alpha}, \tag{10}$$

where $\underline{u}_0^{k\alpha}$ are the nodal positions in the reference configuration, $h^\alpha(\eta)$ the shape functions used in the discretization of the beam element, $\eta \in [0,1]$ a non-dimensional parameter indicating the location of a material particle along the beam axis in the reference configuration, and α an integer varying from 0 to N, the number of nodes in the beam element. Summation over all nodes is implied by repeated α indices. The formulation of nonlinear beam elements is detailed in [3]. Body l can be a rigid or flexible element of the system. The position vector of a node point of this body is denoted $\underline{u}_0^l$ in the reference configuration.

After deformation, the position vector of a point on the beam becomes

$$\underline{P}^k(\eta) = h^\alpha(\eta)\ (\underline{u}_0^{k\alpha} + \underline{u}^{k\alpha}), \tag{11}$$

where $\underline{u}^{k\alpha}$ are the nodal displacement vectors. Similarly, the position vector of the node on body l is

$$\underline{P}^l = \underline{u}_0^l + \underline{u}^l, \tag{12}$$

where $\underline{u}^l$ is the nodal displacement vector. The kinematic constraint associated with the condition of body l freely sliding over the flexible beam is

$$\underline{\mathcal{C}} = \underline{P}^k(\eta) - \underline{P}^l = 0. \tag{13}$$

The parameter η which determines the location of contact between bodies k and l is, of course, a time varying unknown of the problem. Here again, this constraint is enforced via the Lagrange multiplier technique. The corresponding forces of constraint $\underline{\mathcal{F}}^c$ are readily obtained as

$$\delta\underline{\mathcal{C}}^T \cdot \underline{\lambda} = \begin{bmatrix} \delta\underline{u}^{k\alpha} \\ \delta\eta \\ \delta\underline{u}^l \end{bmatrix}^T \cdot \begin{bmatrix} h^\alpha & \underline{\lambda} \\ h^{\alpha\prime}\ (\underline{u}_0^{k\alpha} + \underline{u}^{k\alpha})^T & \underline{\lambda} \\ - & \underline{\lambda} \end{bmatrix} = \begin{bmatrix} \delta\underline{u}^{k\alpha} \\ \delta\eta \\ \delta\underline{u}^l \end{bmatrix}^T \cdot \underline{\mathcal{F}}^c, \tag{14}$$

where $(.)'$ denotes a derivative with respect to η. Here again, these forces of constraint must be discretized so that the work they perform vanishes exactly. The following discretization is proposed

$$\underline{\mathcal{F}}_m^c = \begin{bmatrix} h_m^\alpha & s\underline{\lambda}_m \\ h_d^\alpha\ (\underline{u}_0^{k\alpha} + \underline{u}_m^{k\alpha})^T & s\underline{\lambda}_m \\ - & s\underline{\lambda}_m \end{bmatrix}, \tag{15}$$

where

$$h_m^\alpha = \frac{h^\alpha(\eta_f) + h^\alpha(\eta_i)}{2}; \quad h_d^\alpha = \frac{h^\alpha(\eta_f) - h^\alpha(\eta_i)}{\eta_f - \eta_i}; \quad \underline{u}_m^{k\alpha} = \frac{\underline{u}_f^{k\alpha} + \underline{u}_i^{k\alpha}}{2}. \tag{16}$$

The work $\mathcal{W}^c$ done by these constraint forces is computed as follows

$$\begin{aligned} \mathcal{W}^c &= s\underline{\lambda}_m^T \left[h_m^\alpha(\underline{u}_f^{k\alpha} - \underline{u}_i^{k\alpha}) + h_d^\alpha[\underline{u}_0^{k\alpha} + \underline{u}_m^{k\alpha}](\eta_f - \eta_i) - (\underline{u}_f^l - \underline{u}_i^l)\right] \\ &= s\underline{\lambda}_m^T \left[h^\alpha(\eta_f)(\underline{u}_0^{k\alpha} + \underline{u}_f^{k\alpha}) - h^\alpha(\eta_i)(\underline{u}_0^{k\alpha} + \underline{u}_i^{k\alpha}) - (\underline{u}_0^l + \underline{u}_f^l) + (\underline{u}_0^l + \underline{u}_i^l)\right] \\ &= s\underline{\lambda}_m^T(\underline{\mathcal{C}}_f - \underline{\mathcal{C}}_i), \end{aligned} \tag{17}$$

Clearly the work done by the discretized constraint forces vanishes if $\mathcal{C}_f - \mathcal{C}_i = 0$. In summary, discretization (15) together with the constraint $\mathcal{C}_f = 0$ leads to the vanishing of the work done by the forces of constraint. This energy preserving formulation can be readily extended to an energy decaying formulation by following the steps outlined in section 4.3 of [2].

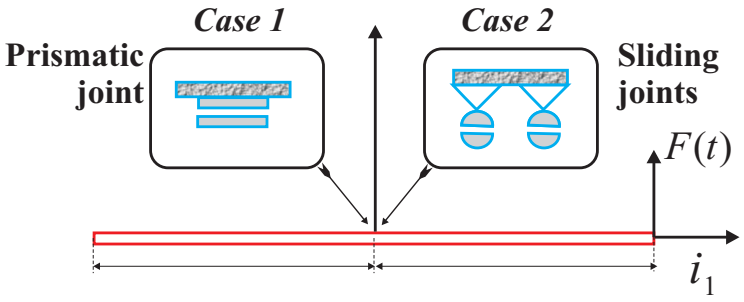

Figure 5: The beam deployment problem.

5 Numerical examples

All the numerical examples presented in this sections used the energy decaying scheme described in [2, 3]. This scheme provides unconditional stability for nonlinear multi-body system involving both prismatic and sliding joints. An automated time step size selection procedure developed in [3] was used to obtain accurate solutions in an efficient manner.

5.1 The beam deployment problem

The first numerical example is the beam deployment problem that will be used to illustrate the dramatic difference between prismatic and sliding joints when flexible bodies are involved. Fig. 5 depicts the problem: a flexible beam of length $L = 2.4\ m$ is subjected to a time varying transverse tip load. Two case will be investigated, denoted *case 1* and *case 2*, respectively. For *case 1*, the beam is supported at mid-span by a prismatic joint clamped to the ground and allowing translation of the beam along the horizontal direction. Relative translation at the prismatic joint is prescribed as $\Delta = 0.3\ (1 - \cos 2\pi t)\ m$. For *case 2*, the beam is supported in a symmetric fashion by two sliding joints separated by a distance $d = 0.24\ m$. The sliding of the left sliding joint is prescribed

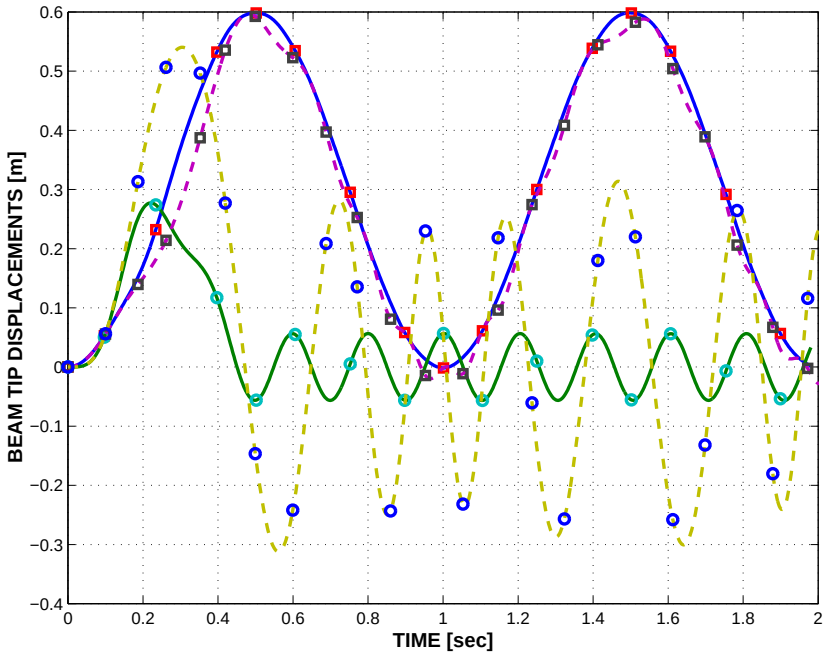

Figure 6: Time history of the beam tip horizontal (□) and transverse (○) deflections. *Case 1*: solid line; *case 2*: dashed line.

as $\eta = 0.325 + 0.125\ \cos 2\pi t$, whereas the sliding of the right sliding joint is unconstrained. Note that the prescribed motion is the same for *case 1* and *2*, the different expressions for Δ and η reflect their different definitions. The beam was modeled with 36 cubic beam elements and this mesh size yielded converged results. Although this fine mesh was not required for *case 1* which converged with 12 elements only, the same fine mesh was used for both cases. The time history of the tip load is $F(t) = 5.0\ (1 - \cos 4\pi t)\ KN$ for $t \leq 0.5\ sec$ and $F(t) = 0$ for $t > 0.5\ sec$. The physical properties of the beam are: axial stiffness $EA = 44.0\ MN$, bending stiffness $EI = 23.0\ KN.m^2$, shearing stiffness $GK = 2.8\ MN$, mass per unit span $m = 1.6\ Kg/m$, and mass moment of inertia per unit span $I = 0.11\ g.m$.

Fig. 6 shows the history of horizontal and transverse displacements of the beam tip for the two cases. The horizontal displacements are almost identical for *case 1* and *2*, as should be expected since the same horizontal translation is prescribed at the joint in both cases. However, the transverse displacements for *case 2* are far larger than those observed in *case 1*. This stems from the completely different constraints imposed by prismatic and sliding joints in the presence of flexible bodies. Indeed, in *case 1*, the beam mid-span point is clamped and translating in a prescribed manner. The tip load bends the right half of the beam only, as depicted in fig. 7 which shows the deflected positions of the beam at various instants in time. In *case 2*, the beam slides with respect to a fixed point in space and, as a result, the tip load bends a variable portion of the beam. As the portion of the beam subjected to bending increases, much larger transverse deflections are obtained. Fig. 6 shows a maximum transverse deflection of about 0.27 *m* for *case 1* as compared to 0.54 *m* for *case 2*. After 0.5 *sec*, the applied load vanishes and for *case 1*, the right half of the beam continues to vibrate at a nearly constant amplitude and frequency. The prescribed translation has little effect on this vibration. In contrast, a variable length of the beam is vibrating in *case 2* resulting in a variable amplitude and frequency response.

Fig. 8 shows the beam mid-span transverse shear forces which are found to be almost one order of magnitude larger for *case 2* as compared to *case 1*. Indeed, for *case 2*, the bending moment induced by the vibrating portion of the beam is reacted by large vertical forces acting in opposite directions

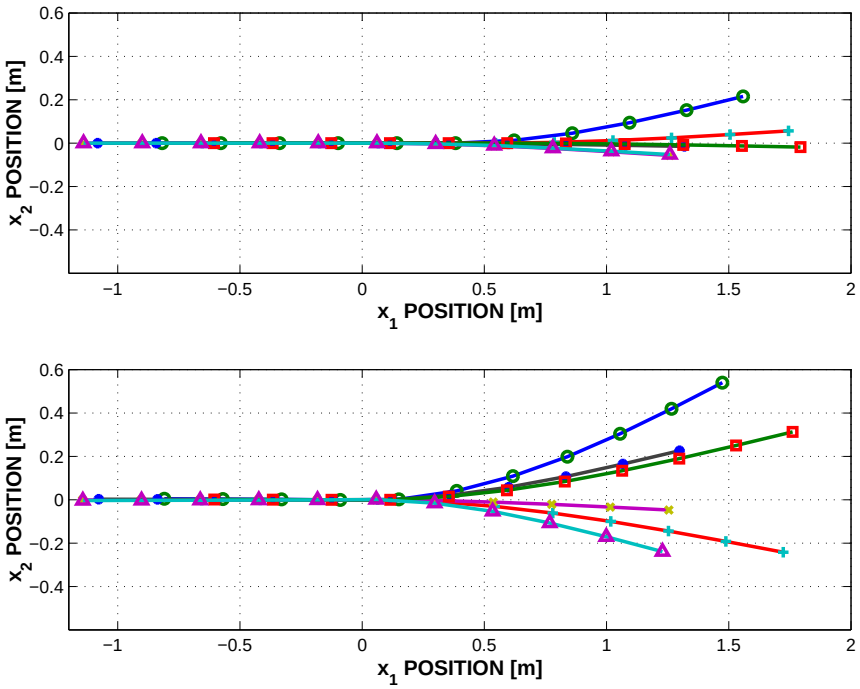

Figure 7: Deflected positions of the beam for *case 1* (top figure) and *2* (bottom figure) at various instants in time: 0.3 (∘), 0.6 (+), 0.9 (x), 1.15 (∗), 1.47 (□), and 1.9 sec (△).

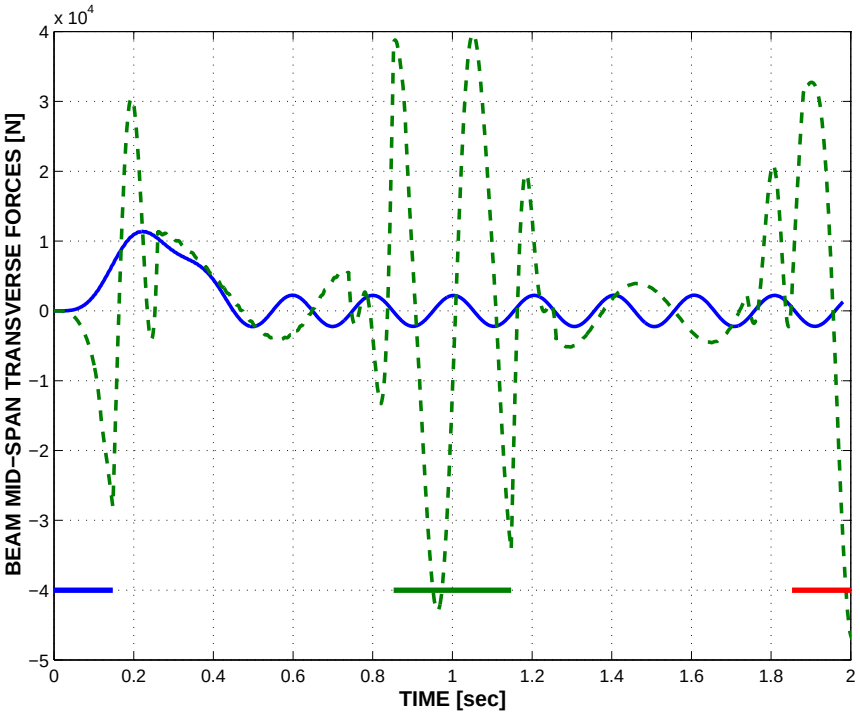

Figure 8: Time history of the beam mid-span transverse shear forces. *Case 1*: solid line; *case 2*: dashed line.

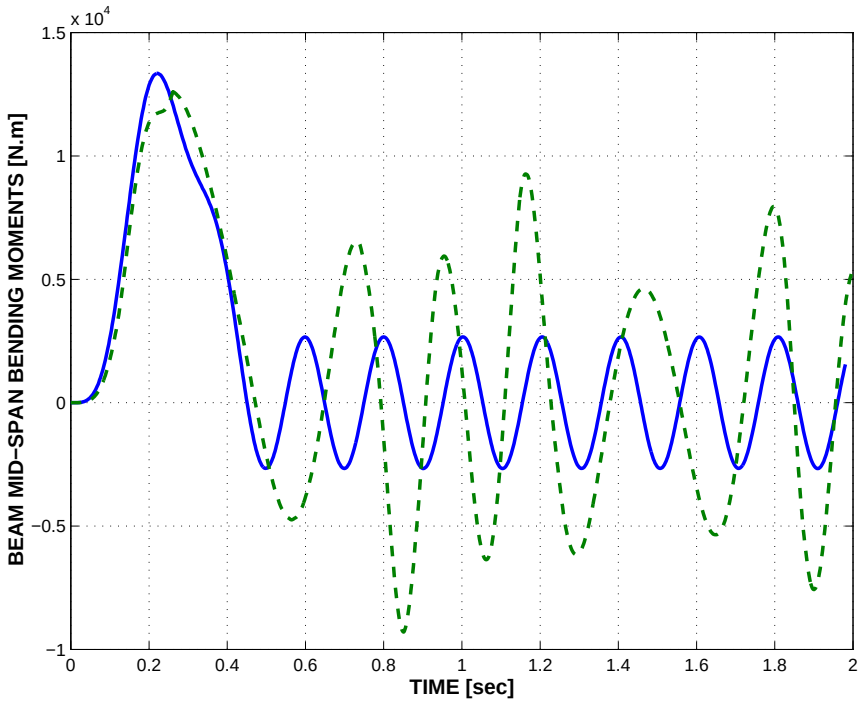

Figure 9: Time history of the beam mid-span bending moments. *Case 1*: solid line; *case 2*: dashed line.

at the two sliding joints. The thick line at the bottom of the figure indicates the time periods when the beam mid-point is between the two sliding joints; the shear force increases dramatically during these periods. Fig. 9 shows the corresponding bending moments at the beam mid-span. Here again much larger amplitudes are observed in *case 2*. All shear forces and bending moments were computed from the derivatives of the shape functions at the Gauss points, then interpolated.

Fig. 10 shows the history of the driving force, positive to the right, required to prescribe the relative displacement at the joints. For *case 1*, this force is relatively small and corresponds the the force required to overcome the inertial forces associated with the beam translation. The high frequency vibrations initially present in the response are beam axial vibrations that rapidly die out due to the numerical dissipation associated with the energy decaying scheme used in the simulation. The driving force history for *case 2* is quite different. As the applied force $F(t)$ grows, it tends to pull the beam out of the sliding joint, and the driving force becomes negative (*i.e.* is oriented to the left) to counteract this pulling. Even after the applied force vanishes (*i.e.* for $t > 0.5$ *sec*), the driving force remains nearly always negative. Indeed, the inertial forces associated with the beam transverse vibration continue to exert a force that tends to pull the beam out of the sliding joint. The large variations in the driving force correlate with the large amplitude vibrations of the beam, see fig. 6. Finally, fig. 11 shows the beam mid-span axial force. For *case 1*, this axial force is equal in magnitude to the driving force, the change of sign is due to sign conventions. For *case 2*, much larger forces are observed again, especially when the beam mid-point is between the sliding joints, as indicated by the thick line at the bottom of the figure.

5.2 The quick return mechanism problem

The second numerical example is a classical quick return mechanism problem involving flexible bodies. Fig. 12 depicts the problem in the initial configuration: a flexible arm of length $L_a = 1.0\ m$ pivots about point B and is connected to a link of length $L_l = 0.25\ m$. The link actuates the shuttle

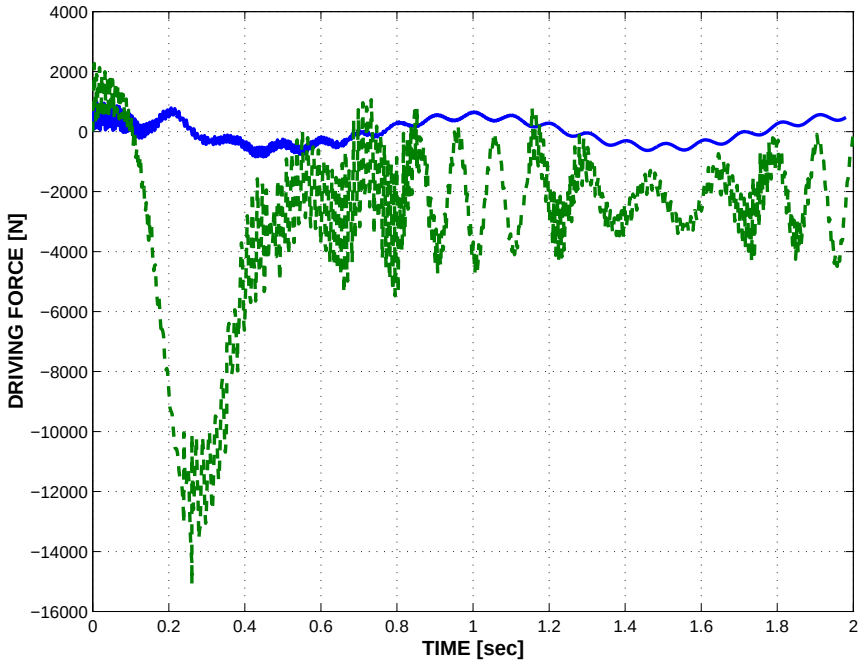

Figure 10: Time history of the driving force. *Case 1*: solid line; *case 2*: dashed line.

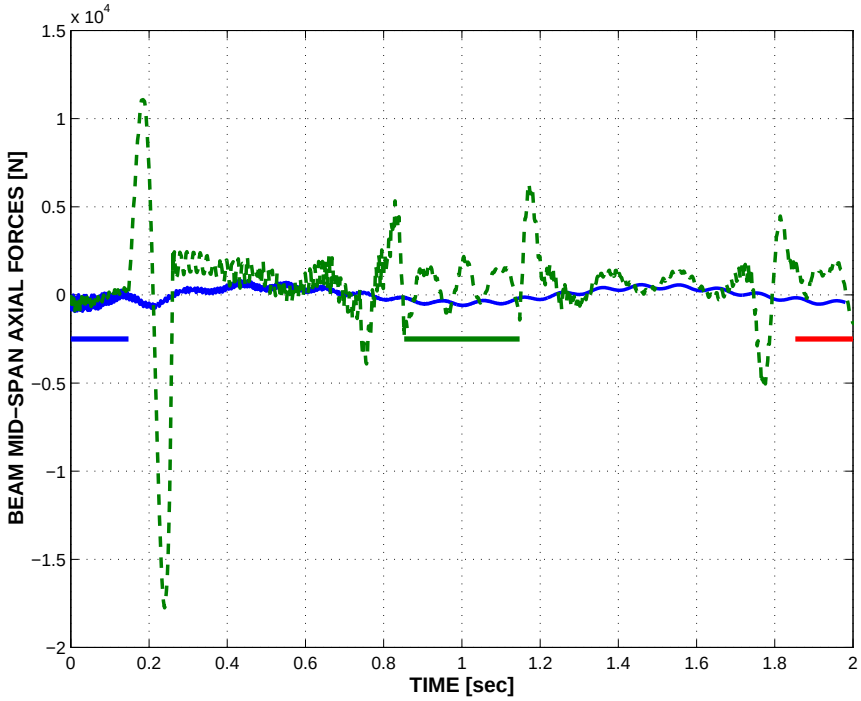

Figure 11: Time history of the beam mid-span axial force. *Case 1*: solid line; *case 2*: dashed line.

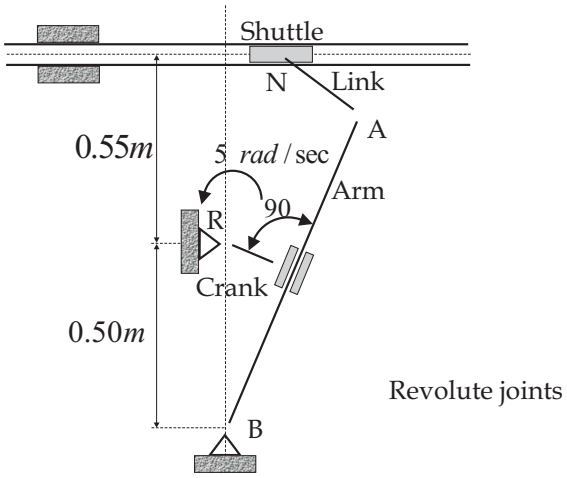

Figure 12: The quick return mechanism problem.

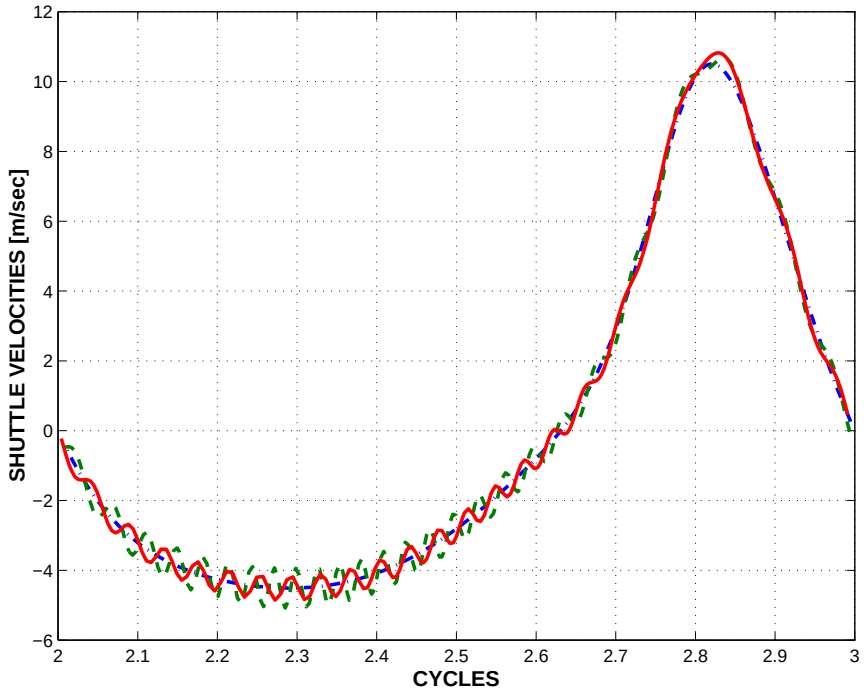

Figure 13: Time history of shuttle velocity. *Case 0:* dashed-dot line; *case 1:* solid line; *case 2:* dashed line.

which is constrained by a prismatic joint to move in the horizontal direction only. A crank of length $L_c = 0.20\ m$ is pinned at R and slides along the arm. Two case will be investigated, denoted *case 1* and *case 2*, respectively. The sliding mechanism is modeled by a prismatic joint which allows relative translation in a direction aligned with the axis of the arm for *case 1*, and by a sliding joint for *case 2*. The angular velocity of the crank root is prescribed to be $\Omega = 5\pi\ rad/sec$.

Although modeled as flexible members by two cubic beam elements each, the crank and link are rather stiff linkages with the following physical properties: axial stiffness $EA = 168.0\ MN$, bending stiffness $EI = 5.0\ MN.m^2$, shearing stiffness $GK = 54.0\ MN$, mass per unit span $m = 6.16\ Kg/m$, and mass moment of inertia per unit span $I = 0.82\ g.m^2$. On the other hand, the arm is a flexible member modeled with 24 cubic elements, and has the following physical properties: axial stiffness $EA = 168.0\ MN$, bending stiffness $EI = 50.0\ KN.m^2$, shearing stiffness $GK = 54.0\ MN$, mass per unit span $m = 6.16\ Kg/m$, and mass moment of inertia per unit span $I = 2.1\ g.m$. The shuttle has a mass $M_s = 2.5\ Kg$ and the sliding mechanism a mass $M_{sm} = 0.31\ Kg$ and mass moment of inertia $I_{sm} = 0.27\ g.m^2$. To provide a reference solution for a rigid body mechanism, a simulation was run with a very stiff arm (bending stiffness $EI = 5.0\ MN.m^2$); this case will be noted *case 0*.

Simulations were run for three complete cycles of the mechanism, and results will be shown for the third cycle, at which time the response is nearly periodic. Fig. 13 shows the shuttle velocity for the three cases. For *case 0*, the response is smooth, in contrast with *cases 1* and *2* which exhibit significant vibrations associated with the elastic nature of the mechanism. The elastic displacements at the arm tip are shown in fig. 14 which depicts the arm tip displacements in a coordinate system attached to the arm at point B. Of course, these elastic displacements vanish for *case 0*. For *cases 1* and *2*, significant elastic displacements are observed, up to about 6 mm. The responses for *cases 1* and *2* are rather similar for the second half of the cycle. During the first half, the amplitude of the elastic displacements for *case 2* are nearly twice those for *case 1*, and the frequency of oscillation is about 30% higher.

A similar behavior is observed in fig. 15 which depicts the arm quarter-point bending moment

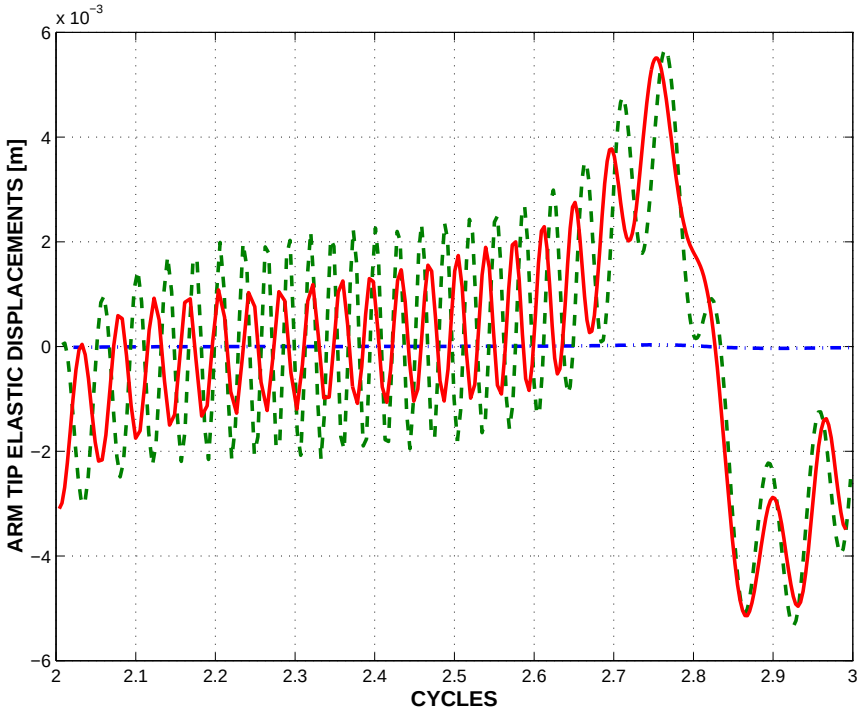

Figure 14: Time history of arm tip elastic displacement. *Case 0:* dashed-dot line; *case 1:* solid line; *case 2:* dashed line.

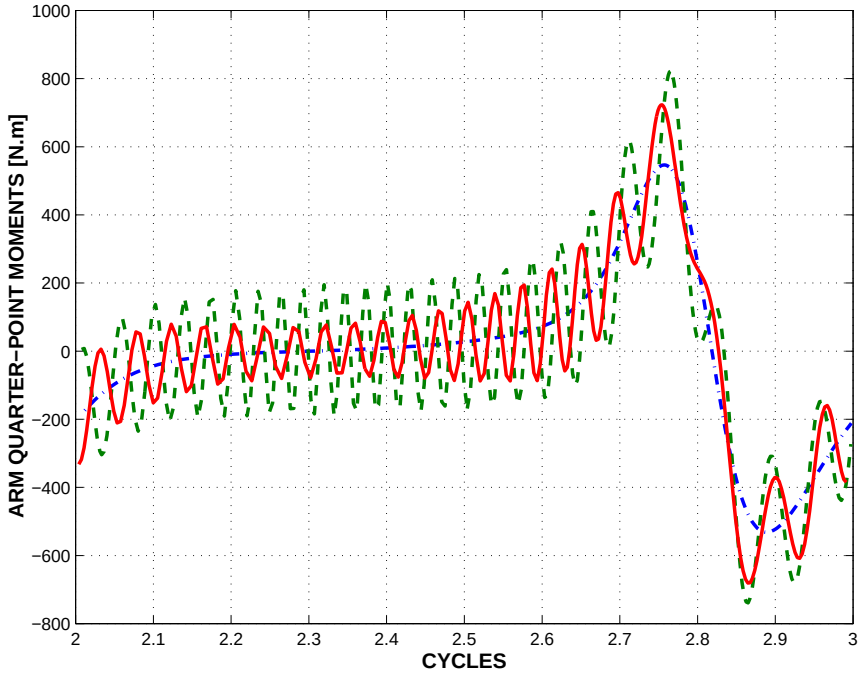

Figure 15: Time history of arm quarter-point bending moment. *Case 0:* dashed-dot line; *case 1:* solid line; *case 2:* dashed line.

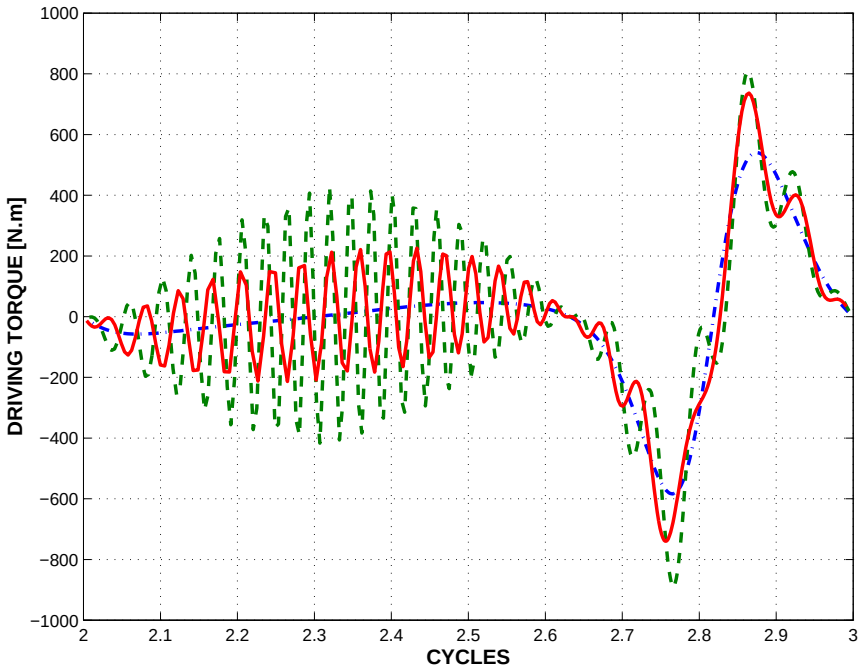

Figure 16: Time history of driving torque. *Case 0:* dashed-dot line; *case 1:* solid line; *case 2:* dashed line.

for the three cases. Here again, higher amplitude and frequency vibrations are observed in the first half of the cycle for *case 2* as compared to *case 1*. Compared to the rigid mechanism, peak moments are about 25% and 42% higher for *cases 1* and *2*, respectively. The torque required to drive the crank at a constant angular velocity is shown in fig. 16. Here again, the type of model for the sliding mechanism primarily affects the first half of the cycle. Peak torques are about 22% and 50% higher for *cases 1* and *2*, respectively, as compared to the rigid mechanism. Finally, figs. 17 and 18 show the crank mid-point bending moments and link mid-point axial forces, respectively. Note again the much higher amplitude and frequency of the response during the first half of the cycle for *cases 2* as compared to *cases 1*.

5.3 The telescoping structure problem

The last numerical example deals with the telescoping structure depicted in fig. 19 which consists of a slider of length $L_s = 2.4\ m$ sliding through a mast of length $L_m = 2.4\ m$. The mast and slider are modeled with 12 and 24 cubic beam elements, respectively. The mast is clamped at point R. An arm of length $L_a = 1.2\ m$, modeled with four cubic beam elements, is connected to the tip of the slider by means of a revolute joint allowing relative rotation of the arm with respect to the slider about an axis aligned with the slider. A mass $M_T = 20\ Kg$ is attached at the tip of the arm. The telescoping mechanism is modeled by a series of seven prismatic or sliding joints equally spaced over the upper half of the mast for *cases 1* and *2*, respectively.

The relative translation of the mid-mast prismatic joint is prescribed as $\Delta = 0.54\ (1-\cos 2\pi t)\ m$. The motion of the corresponding sliding joint is prescribed as $\eta = 0.225\ (1+\cos 2\pi t)$. The relative angular velocity at the revolute joint was prescribed as $\Omega = 2\pi\ rad/sec$. The mast has a circular cross-section with the following physical properties: axial stiffness $EA = 12.0\ MN$, bending stiffness $EI = 30.0\ KN.m^2$, shearing stiffness $GK = 0.6\ MN$, torsional stiffness $GJ = 12.0\ KN.m^2$, mass per unit span $m = 2.0\ Kg/m$, and mass moment of inertia per unit span $I = 6.0\ g.m^2$. Both slider and arm have circular cross-section with the following physical properties: axial stiffness

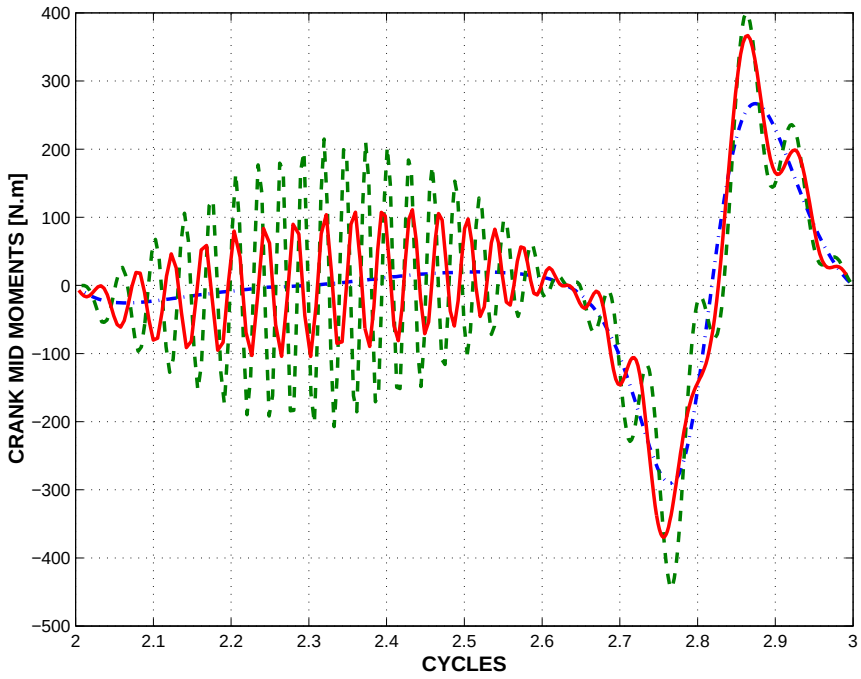

Figure 17: Time history of crank mid-point bending moments. *Case 0:* dashed-dot line; *case 1:* solid line; *case 2:* dashed line.

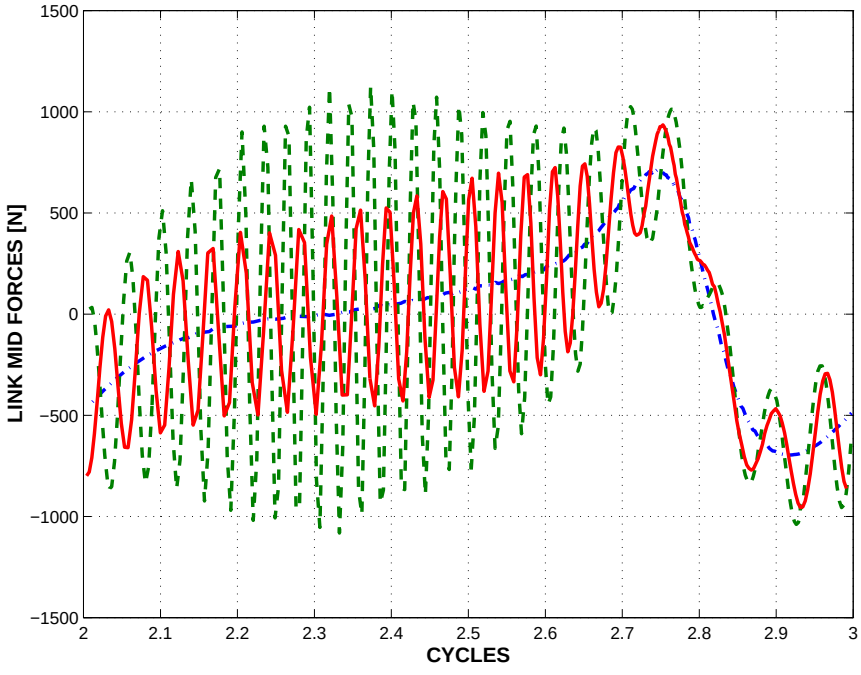

Figure 18: Time history of link mid-point axial forces. *Case 0:* dashed-dot line; *case 1:* solid line; *case 2:* dashed line.

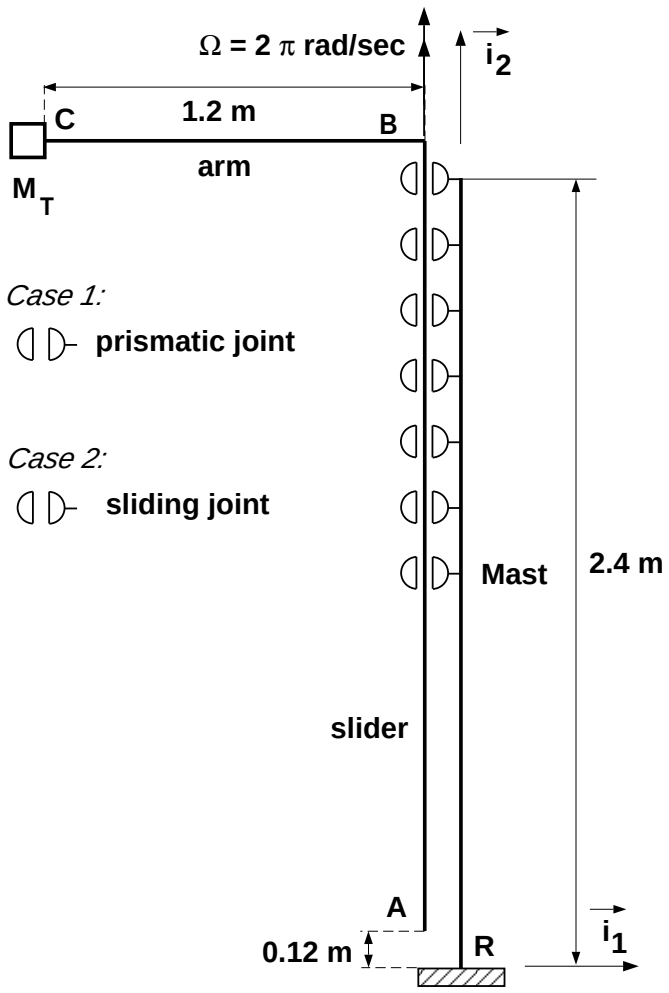

Figure 19: The telescoping structure problem.

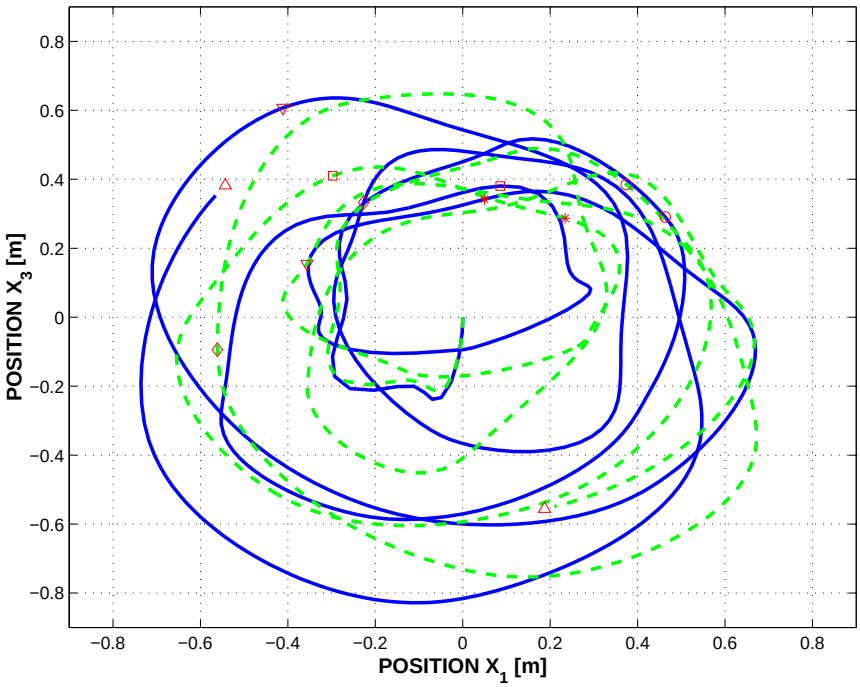

Figure 20: Time history of the mast tip position projected in the $\vec{i}_1$, $\vec{i}_3$ plane. *Case 1:* solid line; *case 2:* dashed line. Time: 0.5 ($\circ$), 1.0 ($\square$), 1.5 ($*$), 2.0 ($\bigtriangledown$), 2.5 ($\diamond$), and 3.0 *sec* ($\bigtriangleup$).

$EA = 9.0\ MN$, bending stiffness $EI = 23.0\ KN.m^2$, shearing stiffness $GK = 0.45\ MN$, torsional stiffness $GJ = 10.0\ KN.m^2$, mass per unit span $m = 1.6\ Kg/m$, and mass moment of inertia per unit span $I = 4.8\ g.m^2$.

The motion of the mast tip projected in the horizontal plane defined by $\vec{i}_1$ and $\vec{i}_3$ is depicted in fig. 20. Although maximum mast deflections are about the same for both cases, as should be expected since identical motions are prescribed at the joints, the details of the response are quite different: after 3 *sec*, the predicted mast tip positions are 1.25 m apart for *cases 1* and *2*. Fig 21 shows the projected trajectory of the slider tip point. Here again, maximum deflections are quite similar, but discrepancies between the trajectories are even more pronounced.

Figs. 22 and 23 show the mast root forces and bending moment, respectively. Similar results are predicted in both cases, as expected since overall motions are similar. However, the forces and moments at the slider mid-point, depicted in figs. 24 and 25, respectively, are sharply different for both cases. The ratio of peak values for *case 2* to those of *cases 1* are -6, $+60$, $+25$, and $+130$ % for the shear force, axial force, bending moment, and torque, respectively. Furthermore, the frequency contents of the responses are very different, much higher frequencies are observed for *case 2*.

6 Conclusions

This paper focused on the modeling of prismatic joints in flexible multi-body systems. In the classical formulation of prismatic joints, kinematic constraints are enforced between the kinematic variables of the two rigid bodies. These constraints express the conditions for relative translation of the two bodies along a body fixed axis, and imply the relative sliding of the two bodies which remain in constant contact with each other at all times. However, these kinematic constraints no longer imply relative sliding with contact when one of the bodies is flexible. In fact, when one body is elastic, the prismatic joint does not enforce contact between the bodies at all times.

A *sliding joint* was introduced that involves kinematic constraints at the instantaneous point of

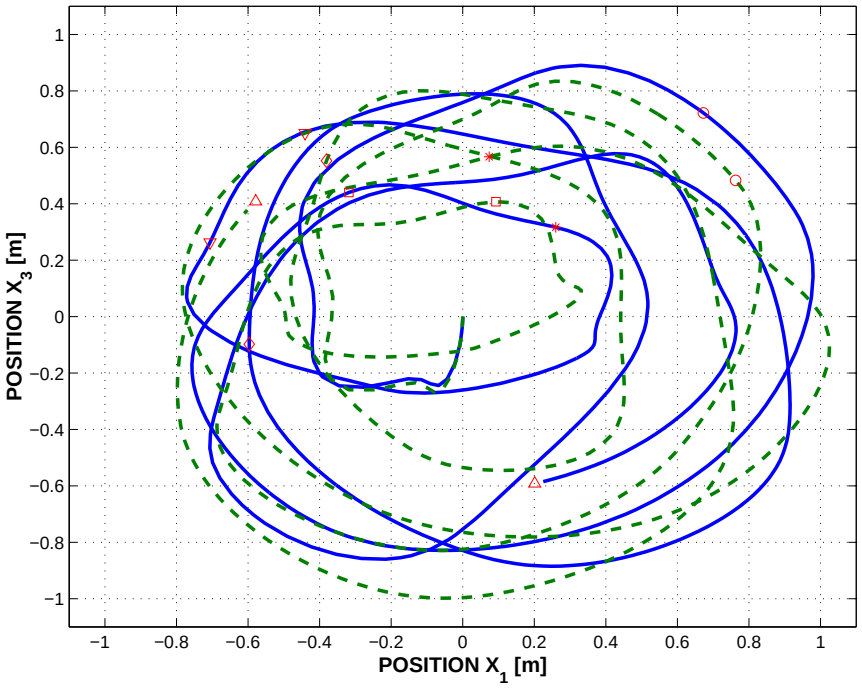

Figure 21: Time history of the slider tip position projected in the $\vec{\imath}_1$, $\vec{\imath}_3$ plane. *Case 1:* solid line; *case 2:* dashed line. Time: 0.5 ($\circ$), 1.0 ($\square$), 1.5 ($*$), 2.0 ($\triangledown$), 2.5 ($\diamond$), and 3.0 *sec* ($\triangle$).

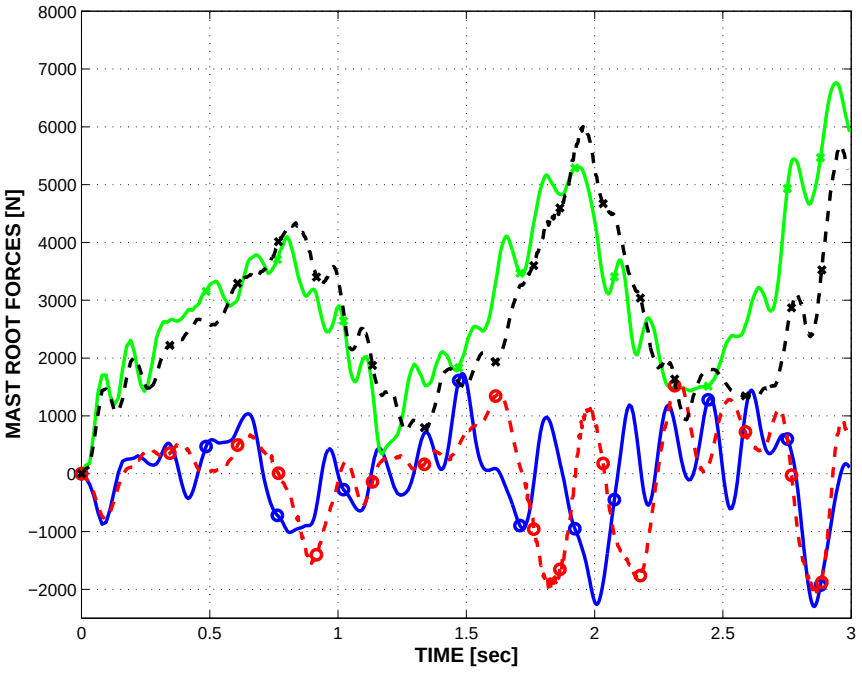

Figure 22: Time history of the mast root forces: axial force ($\circ$), shear force ($\times$). *Case 1:* solid line; *case 2:* dashed line.

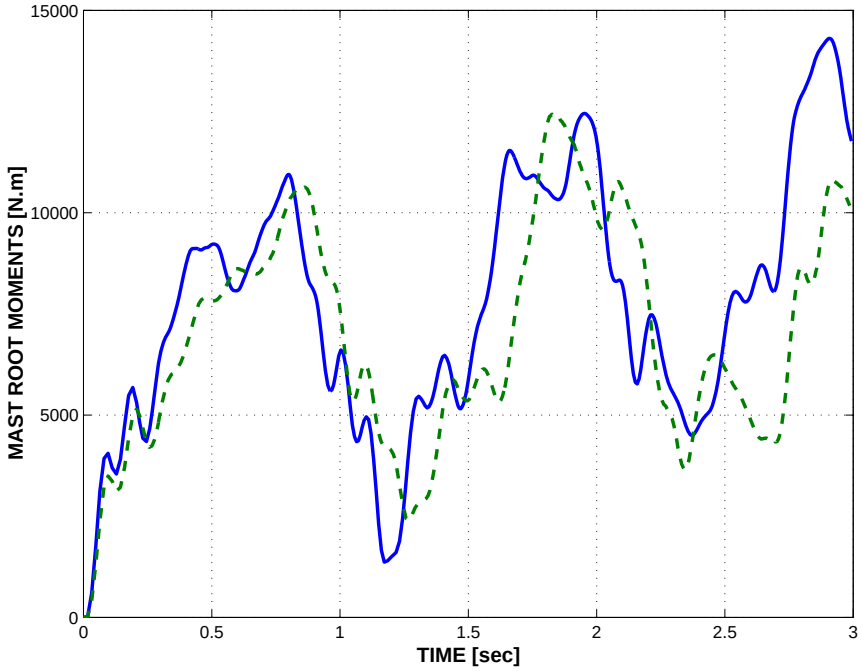

Figure 23: Time history of the mast root bending moments. *Case 1:* solid line; *case 2:* dashed line.

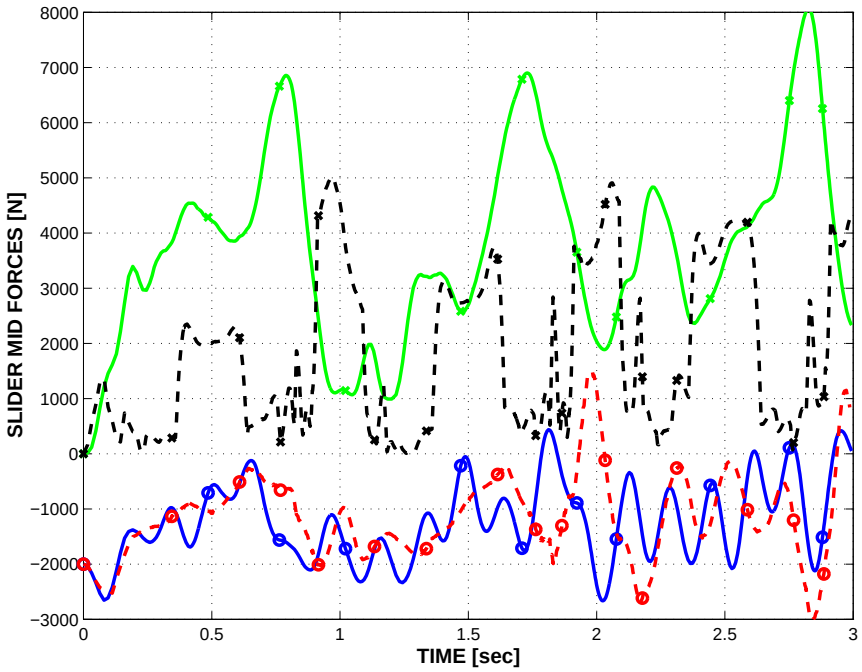

Figure 24: Time history of the slider mid-point forces: axial force ($\circ$), shear force ($\times$). Note: for clarity of the figure, the axial force was shifted down by 2.0 KN. *Case 1:* solid line; *case 2:* dashed line.

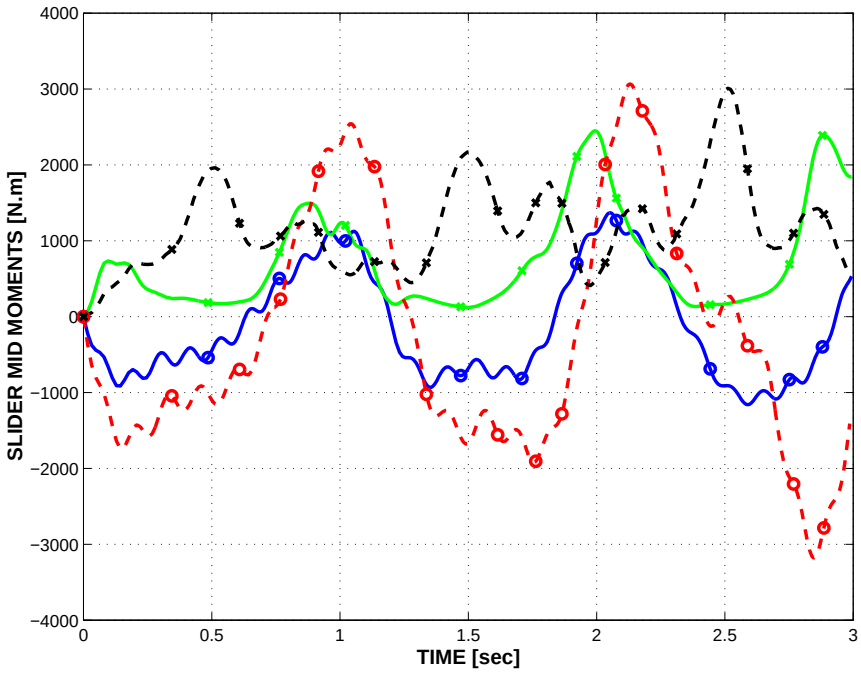

Figure 25: Time history of the slider mid-point moments: torque (∘), bending moment (×). *Case 1:* solid line; *case 2:* dashed line.

contact between the sliding bodies. In the proposed implementation, a specific node of a body is constrained to remain in sliding contact with a beam element. This joint realistically models the piece of hardware that allows a flexible body to be in sliding contact with another. The dynamic behavior of systems with sliding mechanisms was shown to be more complex when the sliding mechanism was modeled by a sliding rather than prismatic joint. This is due to the fact that sliding conditions are applied at a point that moves over the flexible member. As a result, the system configurations becomes truly variable, implying flexible members with time varying natural frequencies.

Various numerical examples are presented that demonstrate the dramatically different behavior of prismatic and sliding joints in the presence of elastic bodies. The proper modeling of the sliding mechanism was shown to be a prerequisite to an accurate prediction of the vibratory loads in a quick return mechanism. The proposed sliding joint enables the modeling of telescoping structures in a rational manner.

References

[1] J.E. Shigley and J.J. Uicker. *Theory of Machines and Mechanisms*. McGraw-Hill Book Company, New York, 1980.

[2] O.A. Bauchau and T. Joo. Computational schemes for nonlinear elasto-dynamics. *International Journal for Numerical Methods in Engineering*, 45(6):693–719, 1999.

[3] O.A. Bauchau. Computational schemes for flexible, nonlinear multi-body systems. *Multibody System Dynamics*, 2(2):169–225, 1998.

[4] C.L. Bottasso and M. Borri. Energy preserving/decaying schemes for non-linear beam dynamics using the helicoidal approximation. *Computer Methods in Applied Mechanics and Engineering*, 143:393–415, 1997.

[5] C.L. Bottasso and M. Borri. Integrating finite rotations. *Computer Methods in Applied Mechanics and Engineering*, 164:307–331, 1998.

[6] T.R. Kane and D.A. Levinson. *Dynamics: Theory and Applications*. McGraw-Hill Book Company, New York, 1985.

Appendix A Rodrigues parameters

A common representation of finite rotations [6] is in terms of Rodrigues parameters $\underline{r} = 2\underline{u}\ \tan\phi/2$, where ϕ is the magnitude of the finite rotation and $\underline{u}$ the components of the unit vector about which it takes place. The following notation is introduced

$$r_0 = \cos^2\frac{\phi}{2} = 1\ /\ (1 + \frac{\underline{r}^T\ \underline{r}}{4}). \tag{A1}$$

The finite rotation tensor R, and the rotation tensor G corresponding to a finite rotation of magnitude $\phi/2$ about the same axis write

$$R(\underline{r}) = I + r_0\ \widetilde{r} + \frac{r_0}{2}\ \widetilde{r}\widetilde{r};\quad G(\underline{r}) = I + \frac{\sqrt{r_0}}{2}\ \widetilde{r} + \frac{r_0}{4(1+\sqrt{r_0})}\ \widetilde{r}\widetilde{r}. \tag{A2}$$

The relationship between angular velocities $\underline{\omega}$ and time derivatives of Rodrigues parameters is $\underline{\omega} = H\ \underline{\dot{r}}$, where

$$H(\underline{r}) = r_0(1 + \frac{1}{2}\ \widetilde{r}). \tag{A3}$$

These operators enjoy the following properties

$$RR^T = I;\quad R\underline{r} = \underline{r};\quad GG^T = I;\quad G\underline{r} = \underline{r};\quad R = GG. \tag{A4}$$

$$\widetilde{r}\ \frac{G+G^T}{2} = \frac{G+G^T}{2}\ \widetilde{r} = G - G^T. \tag{A5}$$

$$\left(I - \frac{\widetilde{r}}{2}\right) G = \left(I + \frac{\widetilde{r}}{2}\right) G^T = \left(\frac{G+G^T}{2}\right)^{-1}. \tag{A6}$$

Appendix B Discretization of finite rotations

Let R_i R_f be the components of the rotation tensor $\mathbf{R}$ at times t_i and t_f, respectively. The incremental rotation $R = R_f R_i^T$ can be divided in two equal parts such that $R = GG$. In this work, the incremental rotation is parameterized with Rodrigues parameters $\underline{r}$. The expressions for $R(\underline{r})$ and $G(\underline{r})$ are given in Appendix A. A mid-point rotation is now easily defined as $R_m = GR_i$. The following relationships summarize the properties of the discretization of the finite rotations

$$\begin{array}{lll} G = R_m R_i^T & G = R_f R_m^T & R = R_f R_i^T \\ G^* = R_0^T R_i^T R_m R_0 & G^* = R_0^T R_m^T R_f R_0 & R^* = R_0^T R_m^T R_f R_i^T R_m R_0. \end{array} \tag{B1}$$

The following operator are extensively used

$$R_a = \frac{R_f + R_i}{2};\quad \mathcal{R}_a = \begin{bmatrix} R_a & 0 \\ 0 & R_a \end{bmatrix};\quad \mathcal{R}_b = \begin{bmatrix} R_a & 0 \\ 0 & HG^T R_m R_0 \end{bmatrix}. \tag{B2}$$